

1 **Spherulite formation in obsidian lavas in the Aeolian Islands, Italy**

2 Running title: Spherulites in obsidian lavas, Aeolian Islands

3

4 Liam A. Bullock^{a, b*}, Ralf Gertisser^a, Brian O'Driscoll^{a, c}

5

6 a) School of Geography, Geology and the Environment, Keele University, Keele, ST5 5BG, UK

7 b) Dept. of Geology & Petroleum Geology, Meston Building, University of Aberdeen, King's College,

8 Aberdeen, AB24 3UE, UK

9 c) School of Earth and Environmental Science, University of Manchester, Williamson Building, Oxford

10 Road, Manchester, M13 9PL, UK

11

12 *Corresponding author.

13 Email liam.bullock@abdn.ac.uk

14

15

16 **ABSTRACT**

17 Spherulites in obsidian lavas of Lipari and Vulcano (Italy) are characterised by spatial, textural and geochemical
18 variations, formed by different processes across flow extrusion and emplacement. Spherulites vary in size from
19 <1 mm to 8 mm, are spherical to elongate in shape, and show variable radial interiors. Spherulites occur
20 individually or in deformation bands, and some are surrounded by clear haloes and brown rims. Spherulites
21 typically contain cristobalite (α , β) and orthoclase, titanomagnetite and rhyolitic glass, and grew over an average
22 period of 5 days.

23 Heterogeneity relates to formation processes of spherulite 'types' at different stages of cooling and
24 emplacement. Distinct populations concentrate within deformation structures or in areas of low shear, with
25 variations in shape and internal structure. CSD plots show differing size populations and growth periods.
26 Spherulites which formed at high temperatures show high degree of elongation, where deformation may have
27 triggered formation. Spherulites formed at mid-glass transition temperatures are spherical, and all spherulites are
28 modified at vapour-phase temperatures. Enhanced undercooling, deformation and post-emplacment modification
29 are therefore pivotal in the development spherulite heterogeneity in obsidian lavas.

30 Key words: Spherulites; Obsidian; Aeolian Islands; Glass Transition; Lipari; Vulcano

31 INTRODUCTION

32 Rhyolitic lava flows and domes on the islands of Lipari and Vulcano (Aeolian Islands, Italy; Fig. 1) provide key
33 information on the formation and modification of spherulites in obsidian lavas. This is in part due to their
34 widespread occurrence, excellent exposure and notable textural and geochemical variations. Despite their
35 common occurrence in obsidian lavas worldwide, questions remain regarding the conditions and processes of
36 spherulite formation. For instance, Watkins et al. (2008) highlight the open questions: on what timescale do
37 spherulites form? When do spherulites begin to form? Do spherulites grow below the glass transition temperature
38 bracket? Clay et al. (2013) further stress the need for a detailed evaluation of the link between spherulite formation
39 and deformation of obsidian lava flows. The preservation of spherulite textures in Aeolian Island obsidian lavas
40 presents a unique opportunity to classify spherulite heterogeneity, and identify processes responsible for their
41 formation and variation.

42 Spherulites are radial fibrous crystallites, usually comprised of silica polymorphs and feldspar (Lofgren,
43 1971a; Swanson, 1977; McArthur et al., 1998; Gardner et al., 2012; Breitzkreuz, 2013). Spherulites are considered
44 to progressively nucleate as a down temperature continuum during syn- and post-emplacement cooling (Clay et
45 al., 2013), originally nucleating in response to an enhanced rate of undercooling brought on by degassing
46 (Kirkpatrick, 1975; Swanson, 1977; Castro et al., 2009; Clay et al., 2013). As well as undercooling, plastic
47 deformation following extrusion has also been suggested as a trigger for the formation of spherulites (Clay et al.,
48 2013), and is particularly emphasised in organic and inorganic compounds and polymers (Shtukenberg et al.,
49 2012). It is also suggested that spherulites form as a hydration and devitrification texture at lower temperatures
50 (Lofgren 1971b; Swanson et al., 1989). Cooling history is a key control on obsidian flow rheology, and
51 subsequently plays a major role in the formation of textures (Gottsmann and Dingwell, 2001a). It has been
52 suggested that spherulite growth can occur above, within, and below glass transition (T_g - 750-600°C), whereby
53 the material changes from liquid-like to solid via a viscoelastic phase transition (Ryan and Sammis, 1981; Manley,
54 1992; Davis and McPhie, 1996; Watkins et al., 2008; Gardner et al., 2012; Clay et al., 2013), meaning that
55 emplacement mechanisms of obsidian lavas may play a key role in spherulite formation.

56 We report here a data set covering twelve obsidian lava flows and domes across Lipari and Vulcano,
57 comprising 4309 individual spherulites, with the focus on the characterisation of their spatial distribution, textural
58 features, and geochemistry. Spherulites have been classified in terms of their physical characteristics, chemical
59 composition and formation origin. Petrographic observations, mineral and glass geochemistry, laser Raman
60 spectroscopy, X-ray diffraction and crystal size distribution methods have been used in order to constrain

61 spherulites formation in obsidian lavas in the Aeolian Islands obsidian suite. These observations and variations
62 provide an indication of different processes of spherulite formation in Aeolian Islands obsidian lavas.

63

64 **GEOLOGICAL BACKGROUND**

65 Recent activity in the central sector of the active Aeolian volcanic province has centred on rhyolitic activity,
66 involving both effusive and explosive phases. On the islands of Lipari and Vulcano, rhyolitic eruptions (often
67 accompanied by mafic enclaves, e.g. De Astis et al., 1997, 2013; Davì et al., 2009, 2010; Piochi et al., 2009; Forni
68 et al., 2013, 2015) have occurred from ~43 ka (Tranne et al., 2002; Gioncada et al., 2003; Lucchi et al., 2010,
69 2013; Forni et al., 2013), with the youngest eruptions occurring in historical time (Lipari - AD 776-1220; Keller,
70 2002; Forni et al., 2013. Vulcano – AD 1888-1890, Mercalli and Silvestri, 1891; De Astis et al., 2013). The oldest
71 rhyolitic lavas are in southern Lipari (Punta del Perciato, Falcone, Monte Giardina and Punta di Costa lava domes;
72 Fig. 2), with younger domes in central and northern Lipari (Castello and Capo Rosso lava domes). At 8.7 ± 1.5
73 ka ago, activity shifted further north on Lipari, with the Pomiciazzo obsidian lava flow extruded from the Vallone
74 del Gabelotto eruptive vent (Bigazzi and Bonadonna, 1973; Lucchi et al., 2010; Forni et al., 2013; Fig. 2). The
75 extrusion of the Forgia Vecchia and Rocche Rosse obsidian lava flows mark the end of this most recent period of
76 activity on Lipari, with the Rocche Rosse obsidian flow dated by archaeomagnetic methods at $1,220 \pm 30$ AD
77 (Tanguy et al., 2003), later revised to $1,230 \pm 40$ AD (Arrighi et al., 2006; Fig. 2). Rhyolitic lava flows and domes
78 have also formed on the neighbouring island of Vulcano (De Astis et al., 1997, 2013; Piochi et al., 2009). The
79 Grotta dei Palizzi obsidian lava flow on the southern flank of the active Fossa cone (Vulcano) has been dated at
80 2.1 ± 0.3 ka (Voltaggio et al., 1995; De Astis et al., 2013; Fig. 2), and, on the northern Fossa flank, the Pietre
81 Cotte obsidian lava flow marks the latest outpourings of the 1739 AD activity (Frazzetta et al., 1984; Fig. 2).

82

83 **SAMPLING AND METHODS**

84 Targeted samples span rhyolitic lava domes ranging in age from 43.0 ± 0.3 ka (Punta del Perciato, Falcone, Monte
85 Giardina, Punta di Costa, Castello and Capo Rosso lava domes on Lipari; Crisci et al., 1991; Lucchi et al., 2010;
86 Forni et al., 2013), younger lava flows (Pomiciazzo, Grotta dei Palizzi, Forgia Vecchia and Rocche Rosse lava
87 flows on Lipari and Vulcano; De Astis et al., 2010; Forni et al., 2013), to 1739 AD activity (Pietre Cotte lava flow
88 on Vulcano; Frazzetta et al., 1984) (Fig. 2). Samples from younger obsidian lavas generally host better-preserved
89 spherulites, and were therefore more extensively sampled. Samples were cut for thin section, and scanned for
90 spherulite crystal size distribution (CSD) analyses. Spherulite outlines were corrected using a polarising

91 microscope. A thickness of one device pixel in width was used. Processing programs *ImageJ* (Schneider et al.,
92 2012), *CSDSlice* (Morgan and Jerram, 2006) and *MATLAB*[®] 6.1 commercial software were used to analyse all
93 particles in a given image, including total spherulite count, spherulite phase abundance and best fit spherulite
94 shape. *CSDSlice* calculates a best fit for the aspect ratios, giving X, Y and Z values (defining the plane in a 3D
95 space). *CSDCorrections 1.37* (Higgins, 2000; 2002; 2006), was used in order to calculate 3D crystal size
96 distributions from 2D data.

97 Glass and mineral major element analysis was undertaken at The Open University (UK) using a
98 CAMECA SX 100 electron microprobe (EMP). The peak count per element for analyses was 15-30 s using a 10-
99 20 μm defocused beam diameter for glass (a 1 μm wide beam used for minerals at a count time of 40 s), with an
100 acceleration voltage of 15 kV and beam current of 10 nA for glass and minerals. Volcanic glass standards (VG-
101 568 and KN-18) were routinely analysed as secondary standards. For X-ray diffraction (XRD) determination of
102 individual compositional phases, spherulites were crushed and sieved, hand-picked using a binocular microscope,
103 and powdered. The coarsely-powdered samples were placed on a flat disk sample holder, gently compressed, and
104 scanned on a Bruker D8 Advance X-ray diffractometer, equipped with a VÅNTEC-500 detector at Keele
105 University (UK), using $\text{CuK}\alpha$ radiation, a scan range from 5 to 90° (2 Theta), a 0.03° (2 Theta) step size and a
106 data collection time of 30 s per step. Samples were prepared for Raman analysis by being cut to wafer-thin
107 sections, ~20 μm in thickness, and polished on both sides. Specific positions in the glassy groundmass, spherulites
108 and brown rims were targeted using a high magnification petrological microscope. Spots of glassy groundmass
109 free of microlites and alteration were targeted. Laser Raman spectroscopy analyses were performed with a Leica
110 microscope coupled to a Renishaw Raman RM1000 system at the University of Southampton (UK), using a
111 Renishaw NIR 780TF semiconductor diode laser (wavelength 780 nm) of power 25 mW. The spectrometer was
112 set up in line with Renishaw recommendations for confocal operation of the spectrometer, calibrated using silicon
113 with a known peak of 520 cm^{-1} . Spectra were obtained using an extended scan between 3700 cm^{-1} and 100 cm^{-1} ,
114 built up of 9 accumulative scans of 10 s, with a spot size of 1-2 μm , and processed using *SigmaPlot 10*.

115

116 **RESULTS**

117 Important characteristics in sampled obsidian lavas include variable deformational structures, degree of
118 devitrification, spherulite morphology, and glass and spherulite geochemistry. These characteristics may impact
119 (or trigger) spherulite nucleation, growth and modification. Crystal Size Distribution methods were utilised in

120 order to assess physical and spatial features, while EMP, XRD and Raman spectroscopy methods provide a means
121 of geochemical characterisation of spherulites and host glass.

122

123 **Textural observations**

124 A number of well exposed lava flows and domes show brittle and ductile deformational fabrics, with multi-scale
125 folding, stretching lineations and sheared spherulites evident (Fig. 3). Such deformational structures often coincide
126 with areas of high spherulite density, and elongate spherulites. Deformational fabrics are widespread across the
127 Rocche Rosse lava flow, whereas deformed fabrics are more restricted to flow frontal regions and flow margins
128 on the Pietre Cotte lava flow (Bullock, 2015). Structures in older lava domes are more difficult to distinguish due
129 to weathering, glass alteration and later pyroclastic coverage.

130 Optical observations of sampled obsidian lavas suggest distinct textural features within the obsidian
131 samples, including widespread spherulites, a glassy groundmass containing microlites, a brown rim and clear halo
132 surrounding most spherulites, and a crystalline mesh-texture found within some spherulites (Fig. 4). Sampled
133 obsidian across the data set is typically glassy black to microcrystalline grey in colour, and variably spherulitic
134 (spherulites predominantly less than 1 mm in diameter, and often defining the planar foliation). Spherulites occur
135 individually, interjoined, and in folds and fractures (Fig. 4). Elongate spherulites can be observed in the Pietre
136 Cotte, Rocche Rosse and Forgia Vecchia lava flows. These elongate spherulites tend to occur within or in close
137 proximity of bands or folded outcrop. Generally, across all flows and domes, large (1-3 mm), spherical spherulites
138 occur individually in zones of low shear or in zones of no banding. Spherulites in the Pomiciazzo and older
139 sampled lavas tend to be much larger than those in younger flows, at 2-3 mm in diameter. The Punta del Perciato
140 lava dome is highly devitrified, and individual spherulites are rarely evident to the naked eye.

141

142 **Spherulite CSDs and growth periods**

143 Clay et al. (2013) show that CSD quantitative textural analysis can be successfully applied to spherulitic
144 samples, as the rate of isothermal spherulitic crystallisation was proven to be log linear in a given growth stage,
145 despite being a non-equilibrium crystallisation process. The use of CSD methods is therefore an effective tool for
146 the interpretation of spherulitic textures. Fifteen CSD plots of spherulites from all lava flows and domes have
147 been produced, with spherulites ranging in size from 0.1 mm (in younger flows), up to 8 mm (in older domes)
148 (Fig. 5). Overall, the sample set shows a kinked regression profile, with steeper, left-hand truncation at lower
149 spherulite sizes, and a shallowing, more uniform regression to larger spherulite populations. The majority of plots

150 show a higher degree of heterogeneity at smaller spherulite sizes, while some plots show little or no deviation
151 from a log-linear profile. Older sampled domes exhibit larger spherulite maximum sizes and wider size ranges.
152 Spherulites below 1 mm in size show a greater degree of complexity, evident by highly non-linear slope
153 regressions. With the exception of samples from Castello, Punta di Costa and Monte Giardina, CSD slopes for
154 sampled flows and domes often deviate from a straight regression. Slopes show a distinct smaller population at
155 <1 mm (Pietre Cotte, Forgia Vecchia, Grotta dei Palizzi, Pomiciazzo, Capo Rosso, Falcone rhyolite and Punta del
156 Perciato), a slope at intermediate sizes of 1-3 mm (Rocche Rosse, Falcone rhyolite, Falcone dacite, Punta del
157 Perciato), and a shallower slope to larger spherulite sizes (Pomiciazzo, Falcone rhyolite, Falcone dacite).

158 Spherulite growth period was calculated using the CSD slope value (determined by *Microsoft Excel*),
159 and assuming a constant spherulite growth rate of 6.33×10^{-7} (calculated by Castro et al. (2008) in obsidian using
160 water concentration profiles). The equation for calculating growth period is:

$$161 \quad \text{Growth period} = -1 \div (\text{slope value} \times \text{growth rate})$$

162 (Marsh, 1988, 1998)

163 The average spherulite growth period across all individual slopes is ~7 days. However, larger spherulites may
164 have formed due to modification/re-crystallisation processes occurring post-emplacment, and therefore may not
165 be a true reflection of primary spherulite growth. Calculating growth periods from smaller and larger size fractions
166 is also difficult as these are typically only defined by two bin sizes. Therefore, small and large size fractions were
167 excluded from calculations, and the slope value was extracted from the main linear body of the CSD profile,
168 defined by three or more bin sizes. If slopes representing smaller and larger spherulites are excluded, the average
169 growth period is ~5 days. Growth periods range across samples from 2 to 11 days (Table 1). A growth period has
170 been calculated for smaller spherulites, though this is only tentatively suggested as the size fraction is defined by
171 two bins. Based on this estimation, smaller spherulites (distinct population <1 mm) formed on average in less than
172 a day. Intermediate spherulites (~1-3 mm) formed over an average of ~5 days (growth periods ranging 2-7 days
173 based on the main body of the CSD profile). Linear slopes from Castello, Punta di Costa and Monte Giardina
174 samples (spherulites typically ~1-3 mm in size) indicate that these spherulites also typically formed over ~5 days,
175 with a range of 4-7 days.

176

177 **Glass and spherulite geochemistry**

178 All glass and mineral compositional data is provided in the Supplementary Appendix. The glass compositions
179 range from rare dacitic/trachytic to typically rhyolitic. The minimum SiO₂ content is ~68 wt% (the Falcone lava

180 dome and Punta del Perciato lava dome) and the maximum SiO₂ content is ~79 wt% (also from the Falcone lava
181 dome) (Fig. 6). The average SiO₂ content for the obsidian glasses is ~75 wt%. Al₂O₃ content varies from ~11 wt%
182 to ~19 wt% (averaging ~13 wt%). Typical Na₂O content is ~3-5 wt%, with slightly higher Na₂O content in the
183 Grotta dei Palizzi lava flow (~5-6 wt%). Brown rims surrounding spherulites show variable enrichment and
184 depletion of SiO₂, Na₂O and K₂O. Generally, spherulites show a high Si content, and a relatively high Al and K
185 content, in specific phases (with a skeletal crystal arrangement). Electron microprobe spot analyses of spherulites
186 reveal a mixture of phases, including glass (with silica values between ~70 wt% and ~78 wt%), quartz and
187 cristobalite (silica content of ~99 wt%), and orthoclase (silica content 60-67 wt%). Spherulites in all sampled
188 obsidian flows and domes contain orthoclase and silica. Plagioclase identified by EMP is primarily albitic, with
189 anorthoclase and oligoclase end members.

190 Examination of Raman spectra for the glassy obsidian groundmass, spherulites (including the
191 microcrystalline mesh-texture) and brown rims show minimal variation in notable peaks (Fig. 7). Spectral results
192 for the haloes show some slight variations. Sharp peaks represent the presence of rare crystalline material, and the
193 broad humped regression is characteristic of amorphous material. Peaks at ~460 cm⁻¹ and ~510cm⁻¹ confirm the
194 presence of silica and orthoclase in spherulites and the glassy groundmass (microlites). There are also notable
195 peaks at ~230 cm⁻¹ and 300 cm⁻¹, with a relatively flat area between 800 cm⁻¹ and 1200 cm⁻¹. Spherulites, mesh-
196 textured interiors and surrounding brown zones show a similar trend to the glassy matrix, confirming the presence
197 of rhyolitic glass in spherulites. Despite the differing optical properties (non-isotropic under crossed polarised
198 light), the brown rims show the characteristic profiles akin to a glass response. The main difference between glass
199 and brown rim results is that although the brown rim shows an amorphous hump appearance, peaks tend to be
200 sharper (more akin to crystalline material). The two major XRD peaks at 21.6° and 27.3° correspond to α-
201 cristobalite and orthoclase feldspar respectively, with minor peaks representing diopside (Fig. 8). There are also
202 peaks suggesting trace amounts of β-cristobalite, quartz, diopside and titanomagnetite, with peaks varying in
203 occurrence and intensity across sampled lavas.

204

205 **DISCUSSION**

206 **Textural variations in spherulites**

207 Results suggest that the sampled obsidian suite across Lipari and Vulcano host spherulite populations of
208 heterogeneous textural characteristics. This is evident in both petrographic observations and kinked CSD profiles
209 (Fig. 6). The upward kinking profile of the CSD plots indicates increasing heterogeneous spherulite nucleation,

210 e.g. faster or denser spherulite nucleation at a later stage. Distinct CSD slopes reflect individual spherulite
211 populations, nucleating and growing at different times and at different rates. This results in texturally
212 heterogeneous spherulite populations within an obsidian lava. In some instances, there is evidence for a downturn
213 at the smaller spherulite sizes (Fig. 6). Petrographic observations suggest that spherulites do not occur below the
214 resolution limit, and smaller spherulites are optically distinct compared to larger spherulites. For spherulites, the
215 upward inflection suggests a clustering or coalescence of large spherulites, the result of localised high nucleation
216 rates and/or the product of prolonged devitrification. Later-stage vapour-phase crystallisation overprinted or re-
217 crystallised earlier formed spherulites, evident by lithophysal textures with an original spherulite in the centre,
218 and resulting in a greater population density of larger spherulites. Samples exhibiting a simple log-linear
219 regression slope indicates a single nucleation event, likely to be the result of constant undercooling. Generally,
220 younger flows have shorter growth periods, and older domes have longer growth periods. This may be a reflection
221 of the size of spherulites being a function of a constant growth rate. However, spherulites are likely to grow at a
222 different rate in a melt compared to those growing in a semi-solid or solid obsidian state. Spherulites may also
223 have grown at different rates from different spherulite-forming processes, i.e. spherulites growing at high
224 temperatures as a response to enhanced undercooling, and spherulites nucleating and growing as a result of
225 deformation. Calculated growth periods for older samples may also take into account the effects of late stage
226 infilling phases (Holzhey, 2001). Notable exceptions to spherulite size being primarily a function of time are large
227 spherulites in samples from the Pomiciazzo lava flow and the Falcone dacite lava dome. As well as time, spherulite
228 growth is primarily a function of temperature and flow rheology. At temperatures approaching melting point,
229 molecular stems settle for longer on the growing crystal face, thus allowing spherulites to grow faster (Lauritzen
230 and Hoffman, 1973; Hoffman et al., 1975; Hoffman and Miller, 1997). Growth may also relate to viscosity, with
231 high T_g viscosities inhibiting diffusion, and thus reducing spherulite growth rate. This suggests that larger
232 spherulites observed in Pomiciazzo and Falcone dacite samples may be a result of differential systems exhibiting
233 prolonged period of higher temperatures and lower viscosities.

234 The regular and highly recognisable occurrence of densely spherulitic glass coinciding with flow
235 deformation, and the uniform occurrence of elongate and/or sheared spherulites, supports a link between flow
236 deformation and spherulite nucleation. Flow-induced crystallisation, also referred to as flow-enhanced nucleation
237 or shear-enhanced nucleation (Kneller, 2002; Graham and Olmsted, 2009), is a well understood phenomenon in
238 polymer sciences as a trigger for spherulite nucleation, but is thus far a neglected concept in a geological context.
239 Elongation in an extensional flow regime has been cited as a strong stimulus for polymer crystallisation, causing

240 molecules to orient and stretch in the direction of extension, facilitating the process of flow-induced crystallisation
241 (Janeschitz-Kriegl et al., 2003; Kornfield et al., 2002; Stadlbauer et al., 2004). Shear flow can induce
242 crystallisation, requiring very large generation of strain (Derakhshandeh and Hatzikiriakos, 2012). Extension and
243 shear flow-related crystallisation may therefore be applicable in highly deformed obsidian lavas. Nucleation
244 depends on the change of the free energy difference between the crystal and the melt phases; the degree of order
245 in the melt phase increases under shear conditions, and the free energy difference increases. The entropic penalty
246 for crystallisation is lowered and, therefore, the nucleation rate increases (Keller and Kolnaar, 1997; Coccorullo
247 et al., 2008). This leads to a high number density of spherulites as a result of deformation, which is evident in
248 field observations in obsidian lavas. This may suggest that, in obsidian lavas, spherulite nucleation may increase
249 with flow deformation (during flow), and remain constant in areas of low (or no) strain (e.g. in areas unaffected
250 by strain during flow, or following flow cessation). This results in high spherulite populations in areas of high
251 strain (and spherulites may be sheared or elongate as a result), and lower populations of (undeformed) spherulites
252 in zones of low strain, allowed to grow and form more typical spherical shapes.

253 Elongate spherulites (elliptical as opposed to bowtie shaped) spatially found within close proximity to
254 deformational structures in sampled flows and domes may have formed while lava was behaving in a ductile
255 manner (within T_g). This is similar to how vesicles and enclaves preserve lava flow strain, based on their shape
256 and size alteration from spherical to elongate (Polacci and Papale, 1997; Rust et al., 2003; Ventura, 2004; Iezzi
257 and Ventura, 2005). The onset of this spherulite nucleation and growth may therefore have been triggered (or
258 enhanced) by flow-induced crystallisation (i.e. as a result of deformation) at high T_g temperatures. This is
259 supported by polymer experiments whereby flow-induced crystallisation occurs near melting point (above T_g or
260 high T_g transition) (Binsbergen, 1966). The stress created by both spherulite nucleation and that acting due to lava
261 flow emplacement modifies the spherulite shape from spherical to elongate. In zones of high strain, such as at
262 flow margins or where individual flow lobes overlap, spherulites are completely sheared into fully spherulitic
263 bands, or microlite-rich flow bands (which may have resulted from flow-induced crystallisation) became
264 spherulite-rich due to microlites acting as spherulite nuclei. There is also clear evidence for spherulites nucleating
265 and growing within brittle fractures, such as conjugate fractures and tension gashes. This suggests that spherulites
266 have preferentially nucleated in these fractures while the flow is behaving in a brittle manner, i.e. at low or below
267 T_g temperatures in localised regions of flow or due to high strain rate, as a response to deformation.

268

269 **Geochemical variations in spherulites**

270 The presence of high temperature β -cristobalite suggests that spherulites were forming at least higher than the β -
271 α temperature transition (~ 270 - 200°C ; Wright and Leadbetter, 1975; Downs and Palmer, 1994; Swainson and
272 Dove, 1994; Damby et al., 2014), as a quench phenomenon (Ewart, 1971). Spherulites were likely to begin
273 forming early, with high temperature β -cristobalite converting to low temperature α -cristobalite (in some
274 instances, incomplete conversion resulting in both α - and β - cristobalite), with quartz also crystallising at lower
275 temperatures. These phases are identified in the XRD peaks. Variations in the intensity and shift of peaks in the
276 clear surrounding haloes results may suggest some degree of compositional variation (evident in EMP results),
277 and may relate to different processes forming the haloes, e.g. secondary crystallisation infilling (Breitkreuz, 2013),
278 or Fe-redox shift (Castro et al., 2009).

279 Results suggest some depletion and enrichment of major elements within spherulites relative to the glassy
280 matrix, and a surrounding rim. Following initial spherulite growth, cavities at the interface of the spherulite and
281 surrounding material may open out, which act as a nucleation surface for a second phase of crystallisation
282 (Breitkreuz, 2013). Where the surrounding halo does not show a crystalline interior, the surrounding colourless
283 halo may be enriched in OH groups and depleted in ferric iron, produced by a redox front (driven by magnetite
284 crystallisation) that originated from the spherulite margin (Castro et al., 2009). Low-temperature components
285 which are rejected at the crystal-melt interface, assisted by a low diffusion rate, form an impurity layer (Keith and
286 Padden; 1963; Lofgren, 1971b). This impurity layer may be identifiable in Aeolian Islands obsidian samples as
287 the surrounding colourless halo or brown rim evident across all lava bodies. The presence of glass within
288 spherulites is reported here, and also noted elsewhere (e.g. Richnow, 1999; Ryabov and Grib, 2005; Castro et al.,
289 2008; 2009; Seaman et al., 2009; Gardner et al., 2012). Seaman et al. (2009) conclude that the preservation of
290 glass within spherulites highlights the critical influence of water concentration on the likelihood of quenching
291 versus crystallisation during undercooling of a melt. Richnow (1999) also suggests that the presence of glass
292 within spherulites is an indicator of incomplete crystallisation and spherulite formation above T_g temperatures.

293

294 **Processes of spherulite formation in Aeolian Islands obsidian lavas**

295 As rhyolitic lava cooled, it passed from liquid-like behaviour to solid (glass)-like behaviour (Gottsmann and
296 Dingwell, 2001b). Nucleation and spherulite formation originally occurred as a response to undercooling, and
297 continued as a down-temperature growth continuum (Clay et al., 2013). In the majority of sampled lavas,
298 microlites grew first and were later overgrown by spherulites. Therefore spherulites mainly formed at lower
299 temperatures than microlite crystallisation. However, smaller spherulites sometimes show microlites deflected

300 around them, indicating that spherulites grew at higher microlite crystallisation temperatures. Spherulites which
301 exhibit a radial centre and non-radial outer zone preserve evidence for both primary spherulite crystallisation and
302 lithophysae forming processes. Spherulites are often surrounded by a brown rim, but there are smaller spherulites
303 which do not show this rim. These spherulite rims may have formed within or below T_g as a solid state reaction
304 (Castro et al., 2009).

305 Textural observations, geochemistry and CSD plots suggest that multiple spherulite populations exist
306 across obsidian flows and domes on Lipari and Vulcano. Each population can be classified according to their
307 textural heterogeneity (Fig. 9). From the digitised spherulites, a representative shape for each spherulite type was
308 created using the CSDSlice program of Morgan and Jerram (2006). X, Y and Z values were plotted in MATLAB®
309 6.1 in order to provide a representative 3D sphere for each spherulite type (Fig. 9). Here, the X, Y and Z data was
310 scaled with the radius, with the centroid of sphere representing 0 on each of the three axes. The equal square axes
311 allow for direct comparison of representative spherulite type shapes, and show true elongation. Representative
312 shapes show that early, high temperature spherulites are more deformed than later, lower temperature spherulites,
313 peaking at high T_g temperatures, with deformation waning towards lower T_g temperatures and below. Initial
314 spherulite nucleation and growth may have been triggered by enhanced undercooling above T_g . This results in
315 spherulites with radial interiors. These can be classified as type 1 spherulites. Microlites were deflected by these
316 high temperature spherulites. Type 1 spherulites are typically the smallest spherulite types (responsible for left
317 hand truncation in spherulite CSDs). The formation of spherulites during emplacement at high T_g transition results
318 in elongate (or sheared) spherulites during ductile flow deformation, which are classified here as type 2
319 spherulites. The occurrence of isolated, spherical spherulites (larger than type 1 spherulites) with a brown rim
320 suggests that some spherulites formed in areas of low strain. These are classified as type 3 spherulites. Other
321 spherulites grew at temperatures within and below T_g , and concentrated within fractures or bands (deformational
322 trigger), classified as type 4 spherulites. Hollow, partially-hollow, or spherulites containing tensional voids and
323 cavities later became infilled or re-crystallised, resulting in internal spherulite colour zonation and pockets of
324 crystal phases. These are classified as type 5 spherulites (modification of other spherulite types), and may only
325 partially contain a radial texture or no radial texture at all. During ascent, eruption and emplacement, lava is likely
326 to cross T_g many times, resulting in breaking, flowing and healing in repetitive cycles (Tuffen et al., 2003; Tuffen
327 and Dingwell, 2005; Vasseur et al., 2013). As a result, spherulites types formed concomitantly in different parts
328 of the obsidian lava body, relating to temperature variations and different processes at work (e.g. at higher
329 temperatures in the core of the obsidian lava, or as a result of flow-induced crystallisation).

330 Though spherulite formation is a function of processes such as undercooling and deformation, it is
331 unlikely to be fully time constrained. Repeated fracturing and healing of rhyolite (Gonnermann and Manga, 2003;
332 Tuffen et al., 2003; Tuffen and Dingwell, 2005; Vasseur et al., 2013), and second boiling (separation of a gas
333 from a liquid phase) also occurs (Manley and Fink, 1987; Westrich et al., 1988; Sisson and Bacon, 1999; Tuffen
334 et al., 2012), which may re-initiate crystallisation. Therefore, differing spherulite types may nucleate and form
335 simultaneously (Fig. 10). Rheological properties such as elasticity and temperature are intrinsically linked. Such
336 rheological parameters will differ across lava flows and domes during and after emplacement. It can therefore be
337 assumed that deformation is intrinsically linked with temperature and different spherulite types form at the same
338 time. In an obsidian flow, for instance, it will be cooler at flow margins and hotter in the centre of the flow.
339 Therefore, spherulites forming via high temperature undercooling in one part of obsidian lava (such as the core of
340 the flow) do so concomitantly with spherulites forming during T_g in other parts of the lava (by flow-induced
341 crystallisation at margins). Type 5 spherulites, characterised by modification and filling of cavities, may occur
342 during and after vapour-activity and fracturing. Such recrystallisation textures developed due to primary cooling,
343 and continued throughout the cooling history of the lavas (Kneller, 2002). Repeated fracturing and healing also
344 means that type 4 spherulites cannot be fully time-constrained, but are restricted to areas of flow that are
345 undergoing a brittle flow regime.

346

347 **Spherulite growth and modification**

348 A total of 4309 spherulites were digitised according to their designated type, from samples spanning all sampled
349 lavas (Figs. 9 and 11). Type 3 showed the highest population of spherulites (51.8%). Types 1, 2 and 5 show a
350 similar percentage of the total population (19.3%, 10.1% and 13.4% respectively), and type 4 was the lowest
351 percentage of the total population (5.3%). Despite type 3 spherulites having the highest population of spherulites
352 across samples, type 5 spherulites covered the highest area fraction (43.3%). Types 1 and 4 covered the smallest
353 percentage area fraction (both 3.3%). These results show that types 3 and 5 dominate spherulite populations in
354 obsidian, both in terms of number of spherulites and area (and volume) covered. Smaller spherulites (typically
355 type 1) exhibit the shortest growth period, estimated at less than a day at high T_g /above T_g temperatures. Spherulite
356 types 2 and 3 are considered to have started growing at high T_g temperatures. The average growth period of ~4
357 days is comparable to that calculated for Rocche Rosse spherulites (also 4 days) at temperatures $\geq 800^\circ\text{C}$ by Clay
358 et al. (2013). Type 5 (larger spherulites) have longer calculated growth periods, but processes of modification/re-
359 crystallisation may be responsible larger crystal sizes, independent of growth period. Type 4 spherulites are often

360 spatially restricted, and thus growth periods were not calculated. This is further substantiated by plots of individual
361 spherulite populations and histograms in Fig. 11. Figs. 11c-h show that types 3-5 are skewed towards more
362 spherical spherulites, while types 1 and 2 (in particular, type 2) show a more even (and elongate) distribution.
363 Type 1 (high temperatures above T_g) spherulites show some elongation, while type 2 spherulites (high T_g
364 temperatures) show the greatest degree of elongation. Spherulite types 3-5 show a more ideal spherical shape.
365 These observations demonstrate some shape variation within each type, and that flow deformation was at its peak
366 at high T_g temperatures, evident by highly deformed type 2 spherulites.

367

368 CONCLUSIONS

369 Examination of spherulites across the exceptionally-preserved obsidian lava domes and flows of Lipari and
370 Vulcano show textural and geochemical heterogeneity, a result of different spherulite-forming processes.
371 Spherulites grew from 2 to 11 days across flows and domes, with an average growth period of 5 days. Processes
372 occur pre-, syn- and post-emplacment, across glass transition temperatures (T_g). This results in five categorised
373 spherulite types:

- 374 • Type 1 spherulites – small, radial and slightly deformed spherulites, formed due to high degrees of
375 undercooling at high T_g transition temperatures or above.
- 376 • Type 2 spherulites – elongate spherulites with a surrounding brown rim, forming due to deformation
377 (tend to form in shear zones) and/or enhanced undercooling.
- 378 • Type 3 spherulites – large, spherical spherulites, often occurring individually in zones of low shear,
379 formed by enhanced undercooling or deformation in low T_g transition or below.
- 380 • Type 4 spherulites – concentrated within fractures and faults, indicating that these formed following
381 solid state deformation.
- 382 • Type 5 spherulites – partially- or fully-modified spherulites and lithophysae, with a non-radial
383 interior, formed by vapour-infilling (low T_g transition or below).

384 Observations highlight the role of enhanced undercooling, deformation, flow-induced crystallisation, and
385 post-emplacment modification in the development of spherulites across T_g temperatures, and considerable
386 spherulite heterogeneity in obsidian lavas.

387

388 ACKNOWLEDGMENTS

389 The authors wish to gratefully acknowledge Andy Tindle (The Open University) for assistance with EMP
390 analyses, and Richard Darton and David Evans (Keele University) for assistance with XRD and Raman analyses.
391 LAB is grateful to Sophie Blanchard for support with MATLAB. The authors acknowledge support from Keele
392 University, and grants from the Mineralogical Society (UK and Ireland) and Volcanic and Magmatic Studies
393 Group. The authors wish to acknowledge Silvio Mollo and Francesca Forni for their detailed and helpful
394 comments to the manuscript.

395

396 REFERENCES

397 Arrighi S., Tanguy J., Rosi M., 2006. Eruptions of the last 2200 years at Vulcano and Vulcanello (Aeolian Islands,
398 Italy) dated by high-accuracy archaeomagnetic. *Physics of the Earth and Planetary Interiors* 159, 225-
399 233.

400

401 Bigazzi G. and Bonadonna F.P., 1973. Fission track dating of the obsidian of Lipari Island (Italy). *Nature* 242,
402 322-323.

403

404 Binsbergen F.L., 1966. Orientation-induced Nucleation in Polymer Crystallization. *Letters to Nature* 211, 516-
405 517.

406

407 Breitzkreuz C., 2001. Introduction to physical volcanology and volcanic textures. CVT Short course, TU
408 Bergakademie Freiberg, Germany.

409

410 Breitzkreuz C., 2013. Spherulites and lithophysae - 200 years of investigation on high-temperature crystallization
411 domains in silica-rich volcanic rocks. *Bulletin of Volcanology* 75, 1-16.

412

413 Bullock L.A., 2015. Structure, emplacement and textural evolution of young obsidian lavas in the Aeolian Islands,
414 Italy. Unpublished PhD thesis, Keele University, UK.

415

416 Castro J.M., Beck P., Tuffen H., Nichols A.R.L., Martin M., 2008. Timescales of spherulite crystallization in
417 obsidian inferred from water concentration profiles. *American Mineralogist* 93, 1816-1822.

418

419 Castro J.M., Cottrell E., Tuffen H., Logan A.V., Kelley K.A., 2009. Spherulite crystallisation induces Fe-redox
420 redistribution in silicic melt. *Chemical Geology* 268, 272-280.
421

422 Clay P.L., O'Driscoll B., Gertisser R., Busemann H., Sherlock S.C. Kelley S.P., 2013. Textural characterization,
423 major and volatile element quantification and Ar–Ar systematics of spherulites in the Rocche Rosse
424 obsidian flow, Lipari, Aeolian Islands: a temperature continuum growth model. *Contributions to
425 Mineralogy and Petrology* 165, 2, 373-395.
426

427 Coccorullo I., Pantani R., Titomanlio, G., 2008. Spherulitic nucleation and growth rates in an iPP under continuous
428 shear flow. *Macromolecules* 41, 9214-9223.
429

430 Crisci G.M., De Rosa R., Esperanca S., Mazzuoli R., Sonnino M., 1991. Temporal evolution of a three component
431 volcanological system: the Island of Lipari (Aeolian Arc, Southern Italy). *Bulletin of Volcanology* 53,
432 207-221.
433

434 Damby D.E., Llewellyn E.W., Horwell C.J., Williamson B.J., Najorka J., Cressey G., Carpenter, M., 2014. The
435 α - β phase transition in volcanic cristobalite. *Journal of Applied Crystallography* 47 (4), 1205-1215.
436

437 Davì M., De Rosa R., Barca, D., 2009. A LA-ICP-MS study of minerals in the Rocche Rosse magmatic enclaves:
438 Evidence of a mafic input triggering the latest silicic eruption of Lipari Island (Aeolian Arc, Italy).
439 *Journal of Volcanology and Geothermal Research* 182, 45-56.
440

441 Davì M., De Rosa R., Holtz F., 2010. Mafic enclaves in the rhyolitic products of Lipari historical eruptions;
442 relationships with the coeval Vulcano magmas (Aeolian Islands, Italy). *Bulletin of Volcanology* 72, 991-
443 1008.
444

445 Davis B., McPhie J., 1996. Spherulites, quench fractures and relict perlite in a Late Devonian rhyolite dyke,
446 Queensland, Australia. *Journal of Volcanology and Geothermal Research* 71, 1-11.
447

448 De Astis G., La Volpe L., Peccerillo A., Civetta L., 1997. Volcanological and petrological evolution of Vulcano
449 island (Aeolian Arc, southern Tyrrhenian Sea). *Journal of Geophysical Research* 102, 8021-8050.
450

451 De Astis G., Lucchi F., Dellino P., La Volpe L., Tranne C.A., Frezzotti M.L., Peccerillo A., 2013. *Geology*,
452 volcanic history and petrology of Vulcano (central Aeolian archipelago). In: Lucchi F., Peccerillo A.,
453 Keller J., Tranne C.A., Rossi P.L. (eds). *The Aeolian Islands Volcanoes*. Geological Society, London,
454 *Memoirs* 37, 281-349.
455

456 Derakhshandeh M., Hatzikiriakos S.G., 2012. Flow-Induced Crystallization of High-Density Polyethylene: The
457 Effects of Shear & Uniaxial Extension. *Rheologica Acta* 51, 315-327.
458

459 Downs R.T., Palmer D.C., 1994. The pressure behavior of α cristobalite. *American Mineralogist* 7 (9), 9-14.
460

461 Ewart A., 1971. Chemical changes accompanying spherulitic crystallization in rhyolitic lavas, central volcanic
462 region, New Zealand. *Mineralogical Magazine* 38, 424-434.
463

464 Forni F., Ellis B.S., Bachmann O., Lucchi F., Tranne C.A., Agostini S., Dallai L., 2015. Erupted cumulate
465 fragments in rhyolites from Lipari (Aeolian Islands). *Contributions to Mineralogy and Petrology* 170, 49,
466 DOI 10.1007/s00410-015-1201-0.
467

468 Forni F., Lucchi F., Peccerillo A., Tranne C.A., Rossi P.L., Frezzotti M.L., 2013. Stratigraphy and geological
469 evolution of the Lipari volcanic complex (central Aeolian archipelago). In: Lucchi F., Peccerillo A.,
470 Keller J., Tranne C.A., Rossi P.L. (eds). *The Aeolian Islands Volcanoes*. Geological Society, London,
471 *Memoirs* 37, 395-469.
472

473 Frazzetta G., La Volpe L., Sheridan M.F., 1984. Evolution of the Fossa cone, Vulcano. *Journal of Volcanology*
474 and *Geothermal Research* 17, 329-360.
475

476 Gardner J.E., Befus K.S., Watkins J., Hesse M., Miller N., 2012. Compositional gradients surrounding spherulites
477 in obsidian and their relationship to spherulite growth and lava cooling. *Bulletin of Volcanology* 74, 8,
478 1865-1879.
479

480 Gioncada A., Mazzuoli R., Bisson M., Pareschi M.T., 2003. Petrology of volcanic products younger than 42 ka
481 on the Lipari-Vulcano complex (Aeolian Islands, Italy): An example of volcanism controlled by
482 tectonics. *Journal of Volcanology and Geothermal Research* 122, 91-220.
483

484 Gonnermann H.M., Manga M., 2003. Flow banding in obsidian: A record of evolving textural heterogeneity
485 during magma deformation. *Earth and Planetary Science Letters* 236, 135-147.
486

487 Gottsmann J., Dingwell D.B., 2001a. Cooling dynamics of phonolitic rheomorphic fall-out deposits on Tenerife,
488 Canary Islands. *Journal of Volcanology and Geothermal Research* 105, 323-342.
489

490 Gottsmann J., Dingwell D.B., 2001b. The cooling of frontal flow ramps: a calorimetric study on the Rocche Rosse
491 rhyolite flow, Lipari, Aeolian Island, Italy. *Terra Nova* 13, 157-164.
492

493 Graham R. S., Olmsted P.D., 2010. Coarse-grained simulations of flow-induced nucleation in semicrystalline
494 polymers. *Physical Review Letters* 103, 115702.
495

496 Higgins M.D., 2000. Measurement of Crystal size distributions. *American Mineralogist* 85, 1105-1116.
497

498 Higgins M.D., 2002. Closure in crystal size distributions (CSD), verification of CSD calculations, and the
499 significance of CSD fans. *American Mineralogist* 87, 171-175.
500

501 Higgins M.D., 2006. *Quantitative textural measurements in igneous and metamorphic petrology*. 1st edition.
502 Cambridge University Press, Cambridge, 270.
503

504 Hoffman J.D., Frolen L.J., Ross G.S., Lauritzen Jr J.I., 1975. On the Growth Rate of Spherulites and Axialites
505 from the Melt in Polyethylene Fractions: Regime I and Regime II Crystallization. Journal of Research
506 01 the Notional Bureau 01 Standards - A. Physics and Chemistry 79A, 671-699.
507

508 Hoffman J.D., Miller R.L., 1997. Kinetic of crystallization from the melt and chain folding in polyethylene
509 fractions revisited: theory and experiment. Polymer 38, 13, 3151-3212.
510

511 Holzhey G., 2001. Contribution to petrochemical-mineralogical characterization of alteration processes within the
512 marginal facies of rhyolitic volcanics of Lower Permian age, Thuringian Forest, Germany. Chemie der
513 Erde 61, 149-186.
514

515 Iezzi G., Ventura G., 2005. The kinematics of lava flows inferred from structural analysis of enclaves: a review.
516 In: Kinematics and dynamics of lava flows. Manga M., Ventura G. (eds). Geological Society of America
517 Special Paper 396, 15-28.
518

519 Janeschitz-Kriegl H., Ratajski E., Stadlbauer M., 2003. Flow as an effective promoter of nucleation in polymer
520 melts: A quantitative evaluation. Rheologica Acta 42, 355-364.
521

522 Keith H.D., Padden F.J., 1963. A Phenomenological Theory of Spherulitic Crystallization. Journal of Applied
523 Physics 34, 2409-2421.
524

525 Keller A., Kolnaar H.W., 1997. Flow induced orientation and structure formation. In: Meijer H.E.H. (ed)
526 Processing of Polymers 18, VCH, New York, 189-268.
527

528 Keller J., 1970. Die historischen Eruptionen von Vulcano und Lipari. Zeitschrift Deutschen Geologischen
529 Gesellschaft 121, 179-185.
530

531 Keller J., 2002. Lipari's fiery past: dating the medieval pumice eruption of Monte Pilato: International Conference
532 'The fire between air and water', UNESCO-Regione Siciliana, Lipari, September 29th-October 2nd, oral
533 presentation.

534
535
536
537
538
539
540
541
542
543
544
545
546
547
548
549
550
551
552
553
554
555
556
557
558
559
560
561
562
563

Kirkpatrick R., 1975. Crystal growth from the melt: a review. *American Mineralogist* 60 (9-10), 798-814.

Kneller E.A., 2002. Preliminary Textural Study of the Proterozoic, Red, Rhyolitic Lava from the St. Francois Mountains, Southeastern Missouri: Textural Description, Origin, & Chronology. Bsc thesis, University of Toledo, USA.

Kornfield J.A., Kumaraswamy G., Issaian A.M., 2002. Recent advances in understanding flow effects on polymer crystallization. *Industrial & Engineering Chemistry Research* 41, 6383-6392.

Lauritzen Jr J.I., Hoffman J.D., 1973. Extension of theory of growth of chain-folded polymer crystals to large undercoolings. *Journal of Applied Physics* 44, 10, 4340-4352.

Le Bas M.J., Lemaitre R.W., Streckeisen A., Zanettin, B., 1986. A Chemical Classification of Volcanic-Rocks Based on the Total Alkali Silica Diagram. *Journal of Petrology* 27, 3, 745-750.

Lofgren G.E., 1971a. Experimentally produced devitrification textures in natural rhyolite glass. *Geological Society of America Bulletin* 82, 111-124.

Lofgren G.E., 1971b. Spherulitic textures in glassy and crystalline rocks: *Journal of Geophysical Research* 76, 23, 5635-5648.

Lucchi F., Tranne C.A., Forni F., Rossi P.L., 2013. Geological map of the island of Lipari, scale 1:10 000 (Aeolian archipelago). In: Lucchi F., Peccerillo A., Keller J., Tranne C.A., Rossi P. L. (eds), *The Aeolian Islands Volcanoes*. Geological Society, London, Memoirs 37.

Lucchi F., Tranne C.A., Rossi P.L., 2010. Stratigraphic approach to geological mapping of the late Quaternary volcanic island of Lipari (Aeolian Archipelago, southern Italy). *The Geological Society of America* 464, 1-33.

564 Manley C.H., 1992. Extended cooling and viscous flow of large, hot rhyolite lavas: implications of numerical
565 modeling results. *Journal of Volcanology and Geothermal Research* 53, 27-46.
566

567 Manley C.H., Fink J.H., 1987. Internal textures of rhyolite flows as revealed by research drilling. *Geology*
568 (Boulder) 15, 6, 549-552.
569

570 Marsh B.D., 1988. Crystal size distributions (CSD) in rocks and the kinetics and dynamics of crystallization I:
571 Theory. *Contributions to Mineralogy and Petrology* 99, 277-291.
572

573 Marsh B.D., 1998. On the interpretations of Crystal Size Distributions in Magmatic Systems. *Journal of Petrology*
574 39, 4, 553-599.
575

576 McArthur A.N., Cas R.A.F., Orton G.J., 1998. Distribution and significance of crystalline, perlitic and vesicular
577 textures in the Ordovician Garth Tuff (Wales). *Bulletin of Volcanology* 60, 260-285.
578

579 Mercalli G., Silvestri O., 1891. Le eruzioni dell'isola di Vulcano, incominciate il 3 Agosto 1888 e terminate il 22
580 Marzo 1890. *Relazione Scientifica. Annali dell'Ufficio Centrale di Meteorologia e Geodinamica* 10, 4,
581 1-213.
582

583 Morgan D., Jerram D.A., 2006. On estimating crystal shape for crystal size distribution analysis. *Journal of*
584 *Volcanology and Geothermal Research* 154, 1-2, 1-7.
585

586 Pichler H., 1976. *Carta geologica dell'Isola di Lipari (scala 1:10,000)*. Firenze, Litografia Artistica Cartografica.
587

588 Piochi M., De Astis G., Petrelli M., Ventura G., Sulpizio R., Zanetti A., 2009. Constraining the recent plumbing
589 system of Vulcano (Aeolian Arc, Italy) by textural, petrological, and fractal analysis: The 1739 A.D.
590 Pietre Cotte lava flow. *Geochemistry, Geophysics, Geosystems*, 10, No Q01009.
591

592 Polacci M., Papale P., 1997. The evolution of lava flows from ephemeral vents at Mount Etna: insights from
593 vesicle distribution and morphological studies. *Journal of Volcanology and Geothermal Research* 76, 1-
594 17.

595

596 Richnow J., 1999. Eruptional and post-eruptional processes in rhyolite domes. Published PhD thesis, University
597 of Canterbury, New Zealand.

598

599 Rust A.C., Manga M., Cashman K.V., 2003. Determining flow type, shear rate and shear stress in magmas from
600 bubble shapes and orientations. *Journal of Volcanology and Geothermal Research* 122, 111-132.

601

602 Ryabov V.V., Grib D.E., 2005. Multiphase dykes: Signature of diverse spreading in the Northern Siberian Craton.
603 *Russian Geology and Geophysics* 46, 5, 471-485.

604

605 Ryan M., Sammis C., 1981. The glass transition in basalt. *Journal of Geophysical Research* 86, 9515-9535.

606

607 Schneider C.A., Rasband W.S., Eliceiri K.W., 2012. NIH Image to ImageJ: 25 years of image analysis. *Nature*
608 *Methods* 9, 671-675.

609

610 Seaman S.J., Dyar M., Marinkovic N., 2009. The effects of heterogeneity in magma water concentration on the
611 development of flow banding and spherulites in rhyolitic lava. *Journal of Volcanology and Geothermal*
612 *Research* 183, 157-169.

613

614 Sisson T.W., Bacon C.R., 1999. Gas-driven filter-pressing in magmas. *Geology* 27, 613-616.

615

616 Shtukenberg A.G., Punin Y.O., Gunn E., Kahr B., 2012. Spherulites. *Chemical Reviews* 112, 1805-1838.

617

618 Stadlbauer M., Janeschitz-Kriegl H., Eder G., Ratajski E., 2004. New extensional rheometer for creep flow at high
619 tensile stress. Part II. Flow induced nucleation for the crystallization of iPP. *Journal of Rheology* 48, 631-
620 639.

621

622 Swanson S., 1977. Relation of nucleation and crystal-growth rate to the development of granitic textures.
623 American Mineralogist 62, 966-978.
624

625 Swanson S., Naney M., Westrich H., Eichelberger J., 1989. Crystallization history of Obsidian Dome, Inyo
626 Domes, California. Bulletin of Volcanology 51, 161-176.
627

628 Swainson I.P., Dove M.T., 1995. Molecular dynamics simulation of alpha- and beta-cristobalite. Journal of
629 Physics: Condensed Matter 7, 1771-1788.
630

631 Tanguy J.C., Le Goff M., Principe C., Arrighi S., Chillemi V., Paiotti A., La Delfa S., Patané G., 2003.
632 Archaeomagnetic dating of Mediterranean volcanics of the last 2100 years: validity and limits. Earth and
633 Planetary Science Letters 211, 111-124.
634

635 Tranne C.A., Lucchi F., Calanchi N., Lanzafame G., Rossi P.L., 2002. Geological map of the Island of Lipari.
636 (Aeolian Islands), Scale 1:10.000. University of Bologna and INGV, LAC, Firenze.
637

638 Tuffen H., Dingwell D.B., 2005. Fault textures in volcanic conduits: Evidence for seismic trigger mechanisms
639 during silicic eruptions, Bulletin of Volcanology 67(4), 370-387.
640

641 Tuffen H., Dingwell D.B., Pinkerton H., 2003. Repeated fracture and healing of silicic magma generate flow
642 banding and earthquakes? Geology 31, 12, 1089-1092.
643

644 Tuffen H., James M., Castro J.M., Schipper I., 2012. Observations of obsidian lava flow emplacement at Puyehue-
645 Cordon Caulle, Chile. Poster session presented at EGU General Assembly, Vienna, Austria.
646

647 Vasseur J., Wadsworth F.B., Lavallée Y., Hess K.U., Dingwell D.B., 2013. Volcanic sintering: Timescales of
648 viscous densification and strength recovery, Geophysical Research Letters 40, 5658-5664.
649

650 Ventura G., 2004. The strain path and kinematics of lava domes: an example from Lipari (Aeolian Islands,
651 Southern Tyrrhenian Sea, Italy). Journal of Geophysical Research 109, B01203.

652

653 Ventura G., 2013. Kinematics of the Aeolian volcanism (Southern Tyrrhenian Sea) from geophysical and
654 geological data. In: Lucchi F., Peccerillo A., Keller J., Tranne C.A., Rossi P. L. (eds), The Aeolian Islands
655 Volcanoes. Geological Society, London, Memoirs 37, 3-11.

656

657 Voltaggio M., Branca M., Tuccimei P., Tecce F., 1995. Leaching procedure used in dating young potassic volcanic
658 rocks by the $^{226}\text{Ra}/^{230}\text{Th}$ method. Earth and Planetary Science Letters 136, 123-131.

659

660 Watkins J., Manga M., Huber C., Martin M., 2008. Diffusion-controlled spherulite growth in obsidian inferred
661 from H_2O concentration profiles. Contributions to Mineralogy and Petrology 157, 2, 163-172.

662

663 Westrich H., Stockman H., Eichelberger J., 1988. Degassing of rhyolitic magma during ascent and emplacement.
664 Journal of Geophysical Research 93, 6503-6511.

665

666 Wnorowska U., 2004. SiO_2 -rich lava complexes: Textures in SiO_2 -rich lava complexes. Oberseminar Geologie,
667 WS 2003/04, Technische Universität Bergakademie Freiberg, Institut für Geologie, Freiberg, Germany.

668

669 Wright A.F., Leadbetter A.J., 1975. The structures of the β -cristobalite phases SiO_2 and AlPO_4 . Philosophical
670 Magazine 31, 1391-1401.

671

672 **FIGURE CAPTIONS**

673 Figure 1. The Aeolian Islands, South Tyrrhenian Sea (Italy), with the islands of Lipari and Vulcano in the centre
674 of the archipelago, straddling the Tindari-Letojanni fault system (Ventura, 2013).

675

676 Figure 2. Geological maps and sample locations of obsidian lavas on Lipari and Vulcano (after Keller, 1970;
677 Pichler, 1976; Lucchi et al., 2010; De Astis et al., 2013; Forni et al., 2013). Units classified by synthems,
678 subsynthems and eruptive history as defined in the geological map of Forni et al. (2013), with synthems shown in
679 bold text, subsynthems in normal text, and eruptive epochs in italics.

680

681 Figure 3. Evidence for spherulitic obsidian coinciding with areas of flow deformation, including (a)-(f)
682 compressive folding (red line in b. highlighting the fold axial plane, and in c. representing fold outline) and (g)-
683 (h) structures resulting from constrictional forces (arrows indicate stretching lineations).

684

685 Figure 4. (a) Small spherulite (Pietre Cotte), with aligned microlites deflected. (b) Spherulites defining flow
686 foliation, heavily concentrated within bands, with few spherulites in zones of low shear (Rocche Rosse). (c)
687 Spherulite with radial centre, mesh-texture near edge, outer clear halo and surrounding brown rim (Falcone
688 rhyolite). (d) Microscopic folding, with folded spherulitic-rich band (Rocche Rosse). (e) Microcrystalline
689 spherulite (non-radial) and ellipsoidal, radial spherulites (Pomiciazzo). (f) Spherulites concentrated within
690 conjugate fracture (Rocche Rosse).

691

692 Figure 5. (a) Combined and (b) individual spherulite crystal size distribution plots for all lavas (with associated
693 error bars). Note higher degree of complexity in slopes at smaller (<1 mm) spherulite sizes, and the shallowing of
694 slope to higher spherulite sizes (smaller spherulites more common in younger lavas, maximum sizes more
695 associated with older samples).

696

697 Figure 6. Total Alkali-Silica (TAS) diagram (adapted from Le Bas et al., 1986) of glass compositions across
698 sampled lavas. The majority of points are clustered together at 73-76 wt% SiO₂ and 7-9 wt% Na₂O + K₂O (shown
699 by red field).

700

701 Figure 7. Raman spectrum and peaks for (a) obsidian glass groundmass, (b) spherulite interiors, (c) brown rims
702 surrounding spherulites, (d) mesh-like textures found in some spherulites and (e) clear haloes immediately
703 surrounding some spherulites.

704

705 Figure 8. X-ray diffraction (XRD) results and peaks for spherulites from sampled lavas. Notable peaks include
706 several α -cristobalite and orthoclase peaks (main constituents), with minor quartz, magnetite, β -cristobalite and
707 diopside peaks, and an overall amorphous regression.

708

709 Fig. 9: Spherulite type classification scheme based on textural characteristics, composition and CSD plots. In the
710 digitised images, red areas represent a primary spherulite phase, blue is a secondary infilling phase and yellow is
711 a reaction rim.

712

713 Fig. 10: Temperature model for the formation of classified types of spherulites. Model demonstrates that spherulite
714 type classification is rheologically controlled, and spherulite types may form simultaneously in different areas of
715 lava (texture process timeline modified from Breitzkreuz, 2001 and Wnorowska, 2004). Indicated T_g range based
716 on previous estimations (Ryan and Sammis, 1981; Manley, 1992; Davis and McPhie, 1996; Watkins et al., 2008;
717 Gardner et al., 2012; Clay et al., 2013).

718

719 Fig. 11: Individual spherulite parameters (categorised by types). (a) Plot of long axis vs. ratio of length and width
720 (W/L) for all spherulites. (b) Representative Fields of long axis vs. W/L ratio, showing that the majority of type 2
721 spherulites are more elongate than other types. (c-g) Histograms for spherulite types and (h) stacked histogram of
722 all types.

723

724

725

726

727

728

729

730

731

732

733

734

735

736

737

738

739 **FIGURES**

740

741 Figure 1

742



743

744

745

746

747

748

749

750

751

752

753

754

755

756

757

758

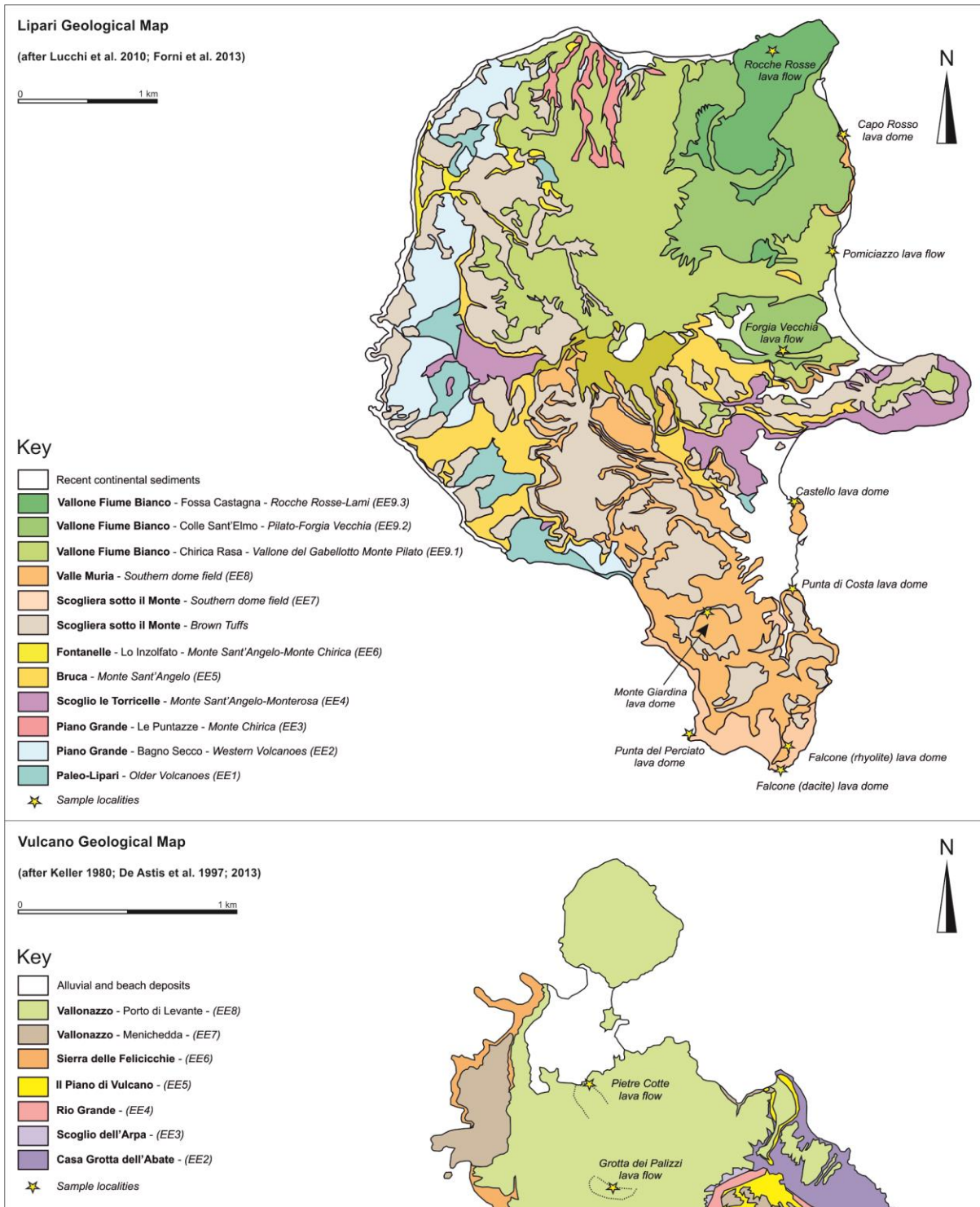
759

760

761

762 Figure 2

763



764

765

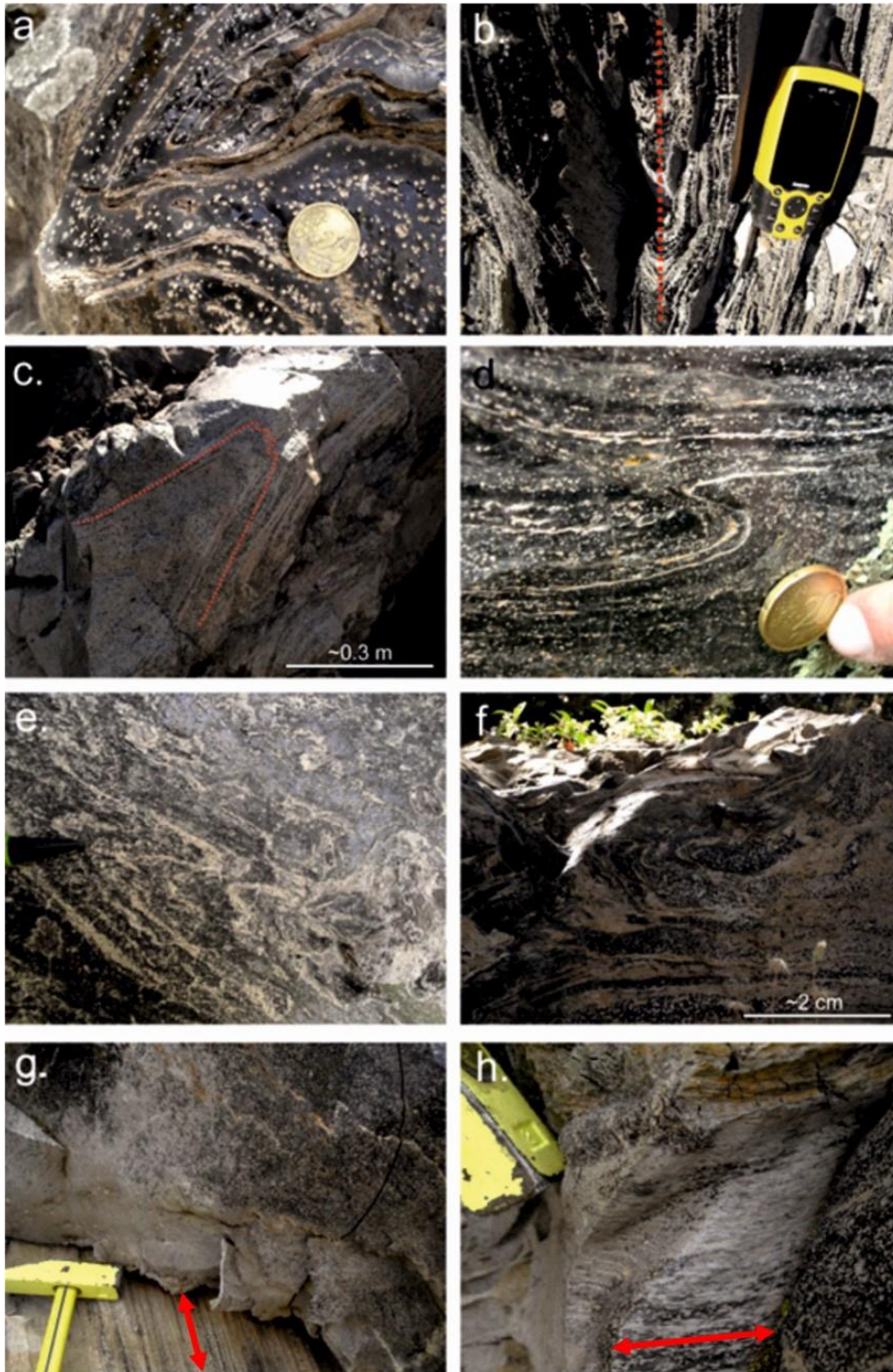
766

767

768

769 Figure 3

770



771

772

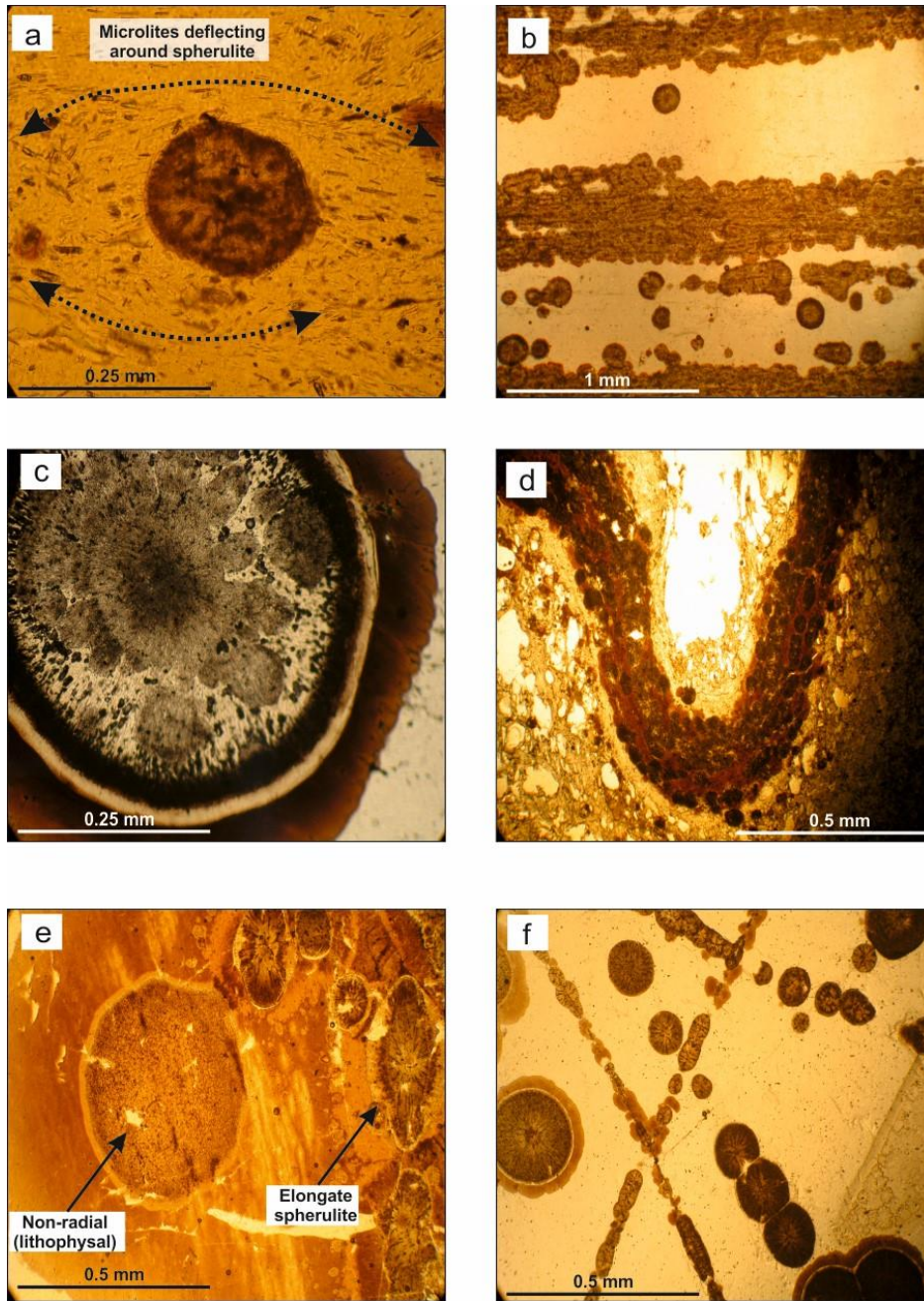
773

774

775

776 Figure 4

777



778

779

780

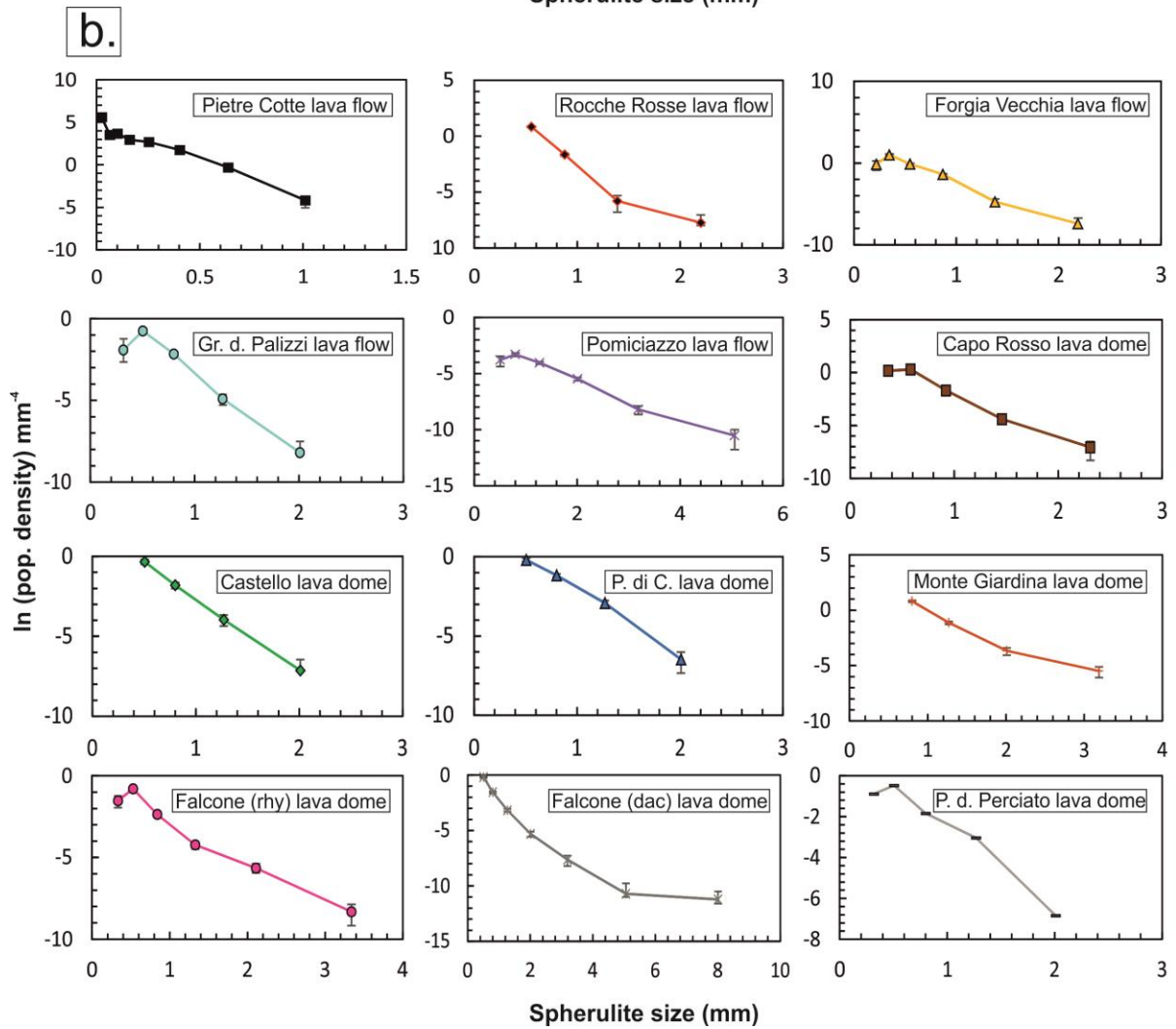
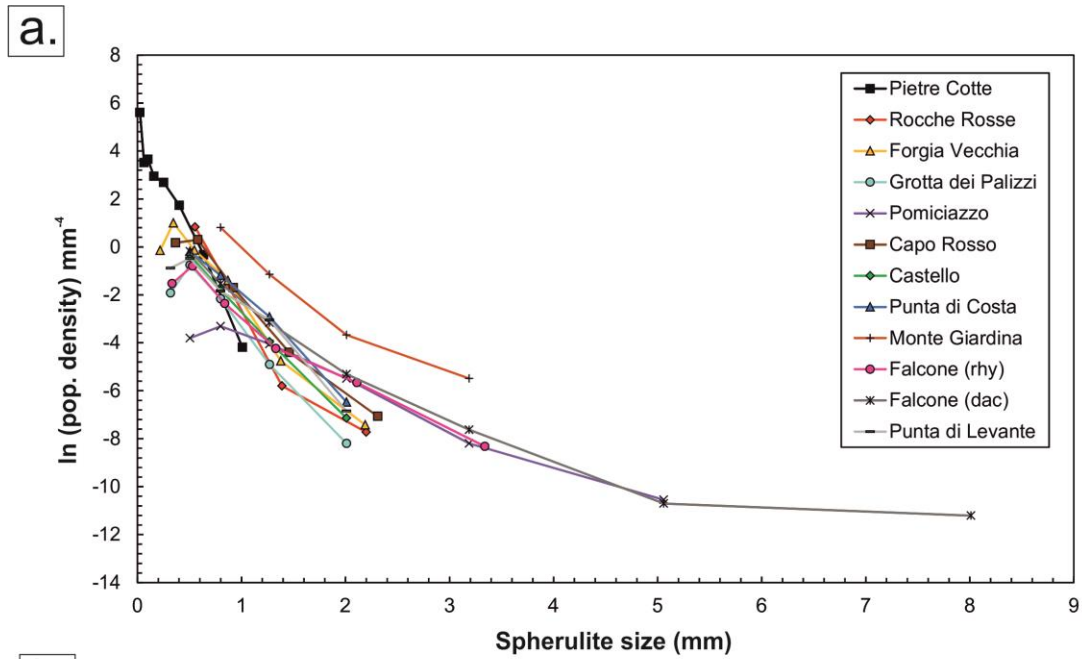
781

782

783

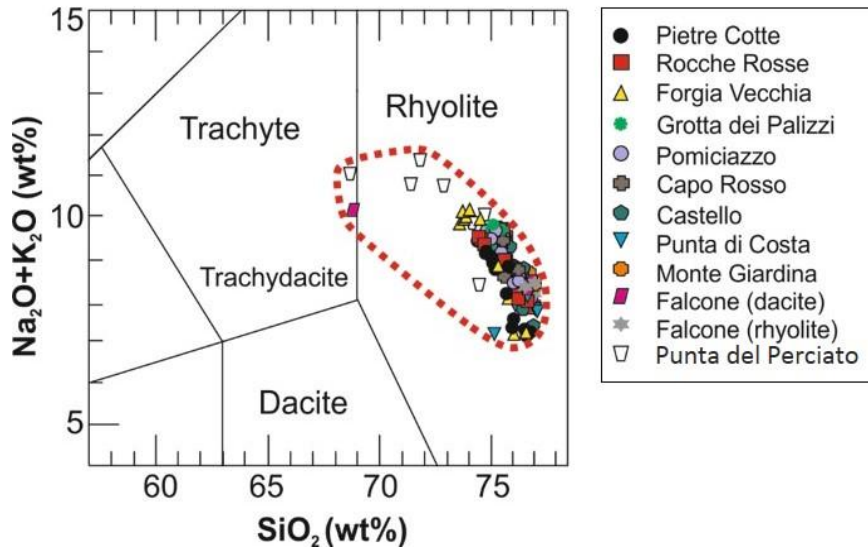
784

785



789 Figure 6

790



791

792

793

794

795

796

797

798

799

800

801

802

803

804

805

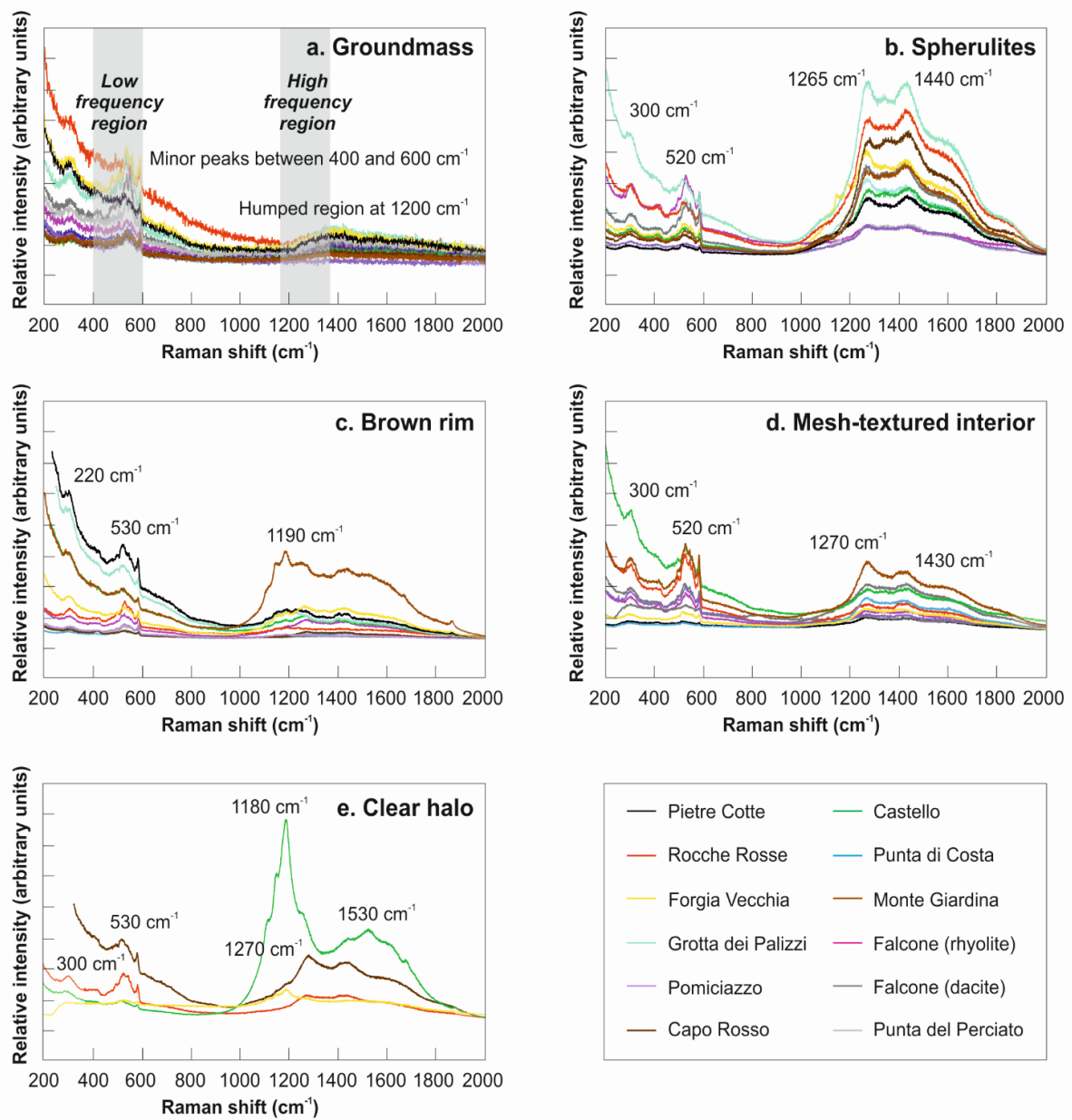
806

807

808

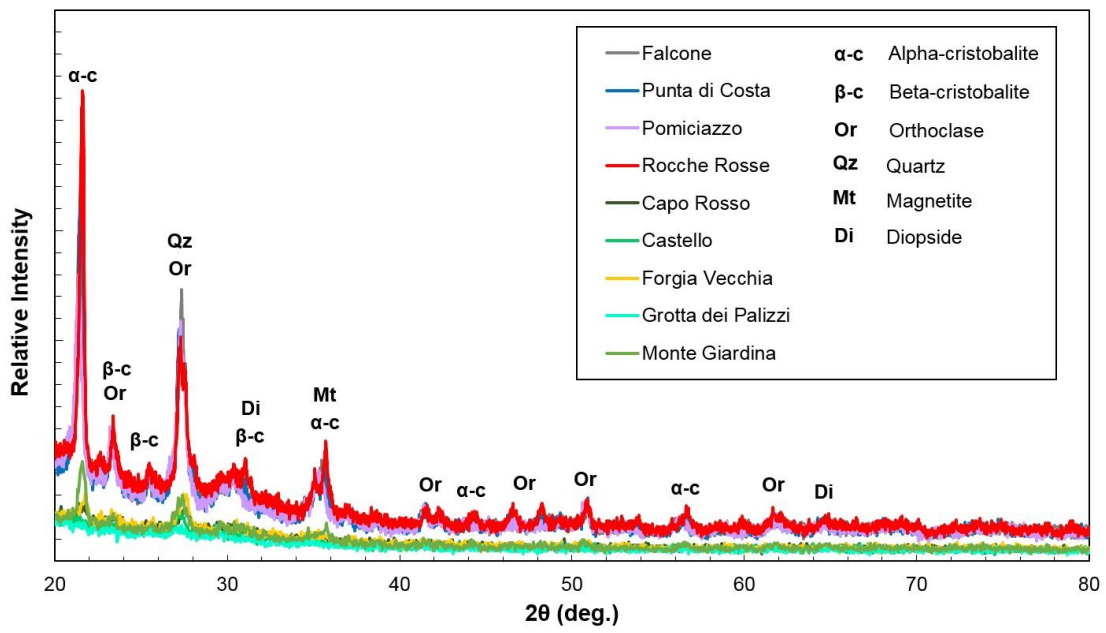
809

810



821 Figure 8

822



823

824

825

826

827

828

829

830

831

832

833

834

835

836

837

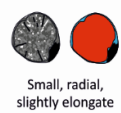
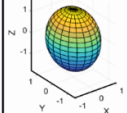
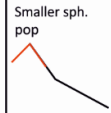

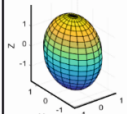


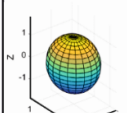

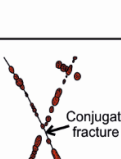
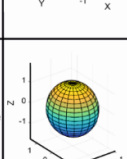


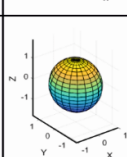
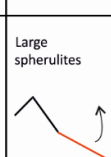
838

839

840

841 Figure 9

842

Type	Image	Representative shape	Typical size	Features	Composition	Growth period	% of total sph.	% of total sph. area	Typical CSD slope	Formation
1	 Small, radial, slightly elongate		< 1 mm	Radial interior, sub-spherical, occasional mesh-textured rim, microlites deflected	a-β cristobalite transition (some β-crist. fixed in matrix), orthoclase, glass, diopside, titanomagnetite	Less than one day	19.3%	3%		Enhanced undercooling at high-T temperatures above T _g (temperatures similar to microlite crystallisation)
2	 Elongate		1-2 mm	Elongate shape, vague radial interior, associated with deformational fabrics, brown rim, mesh-texture	a cristobalite, orthoclase, glass. Zones and pockets of pure crystalline silica	2-7 days	10.2%	13.3%		Constant degree of undercooling and deformational trigger. Nucleation during high T _g temperatures
3	 Radial, large and spherical		1-3 mm	Radial interior, sub-spherical, associated with zones of low shear, clear halo, mesh-textured rim, thick brown rim, microlites unaffected	a cristobalite, orthoclase, glass. Zones and pockets of pure crystalline silica	2-7 days	51.9%	39.4%		Constant enhanced undercooling and deformational trigger (low intensity), mid- to sub-T _g temperatures
4	 Conjugate fracture		<1 mm	Concentrate within joints and fractures, often interjoined, no halo or brown rim, radial and no zonation	a cristobalite, orthoclase, glass	-	5.3%	2.8%		Deformation and preferential nucleation within constrained faults and fractures, below T _g , nucleation and restricted growth (spatially-controlled)
5	 Lack of internal structure		>1 mm	Partially radial or microcrystalline interior, non-continuous or poorly defined spherulite edge, Mesh-like texture	a cristobalite, quartz, orthoclase, glass	-	13.4%	41.7%		Modification of previous types at vapour stage temperatures and below T _g , secondary alteration of spherulites and cavities. Otherwise classified as Lithophysae

843

844

845

846

847

848

849

850

851

852

853

854

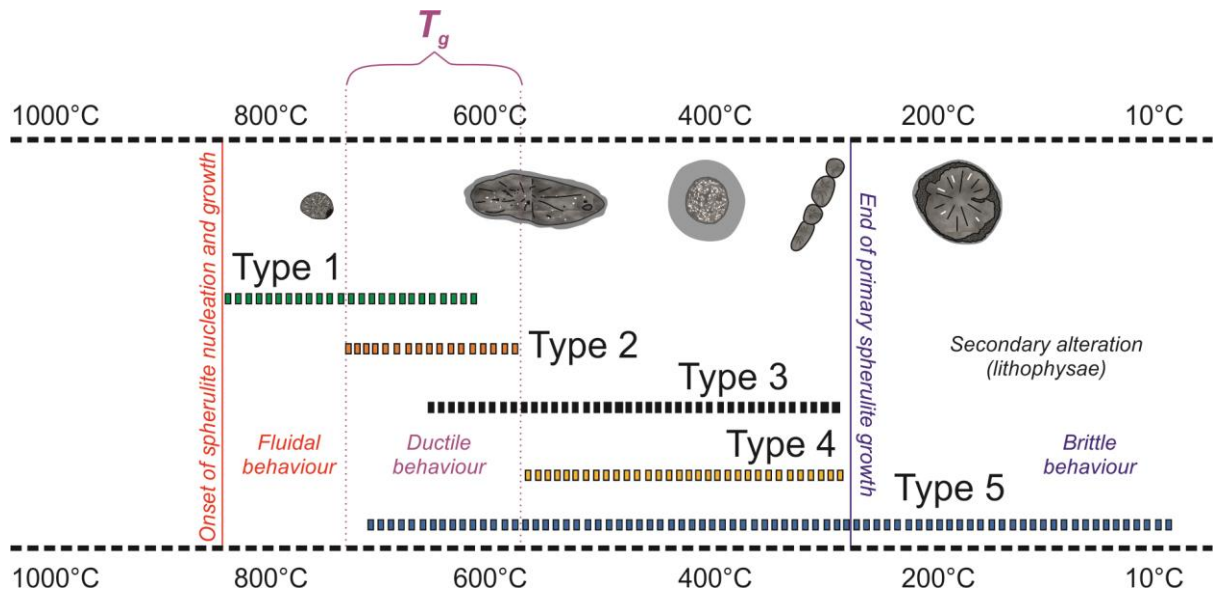
855

856

857

858 Figure 10

859



860

861

862

863

864

865

866

867

868

869

870

871

872

873

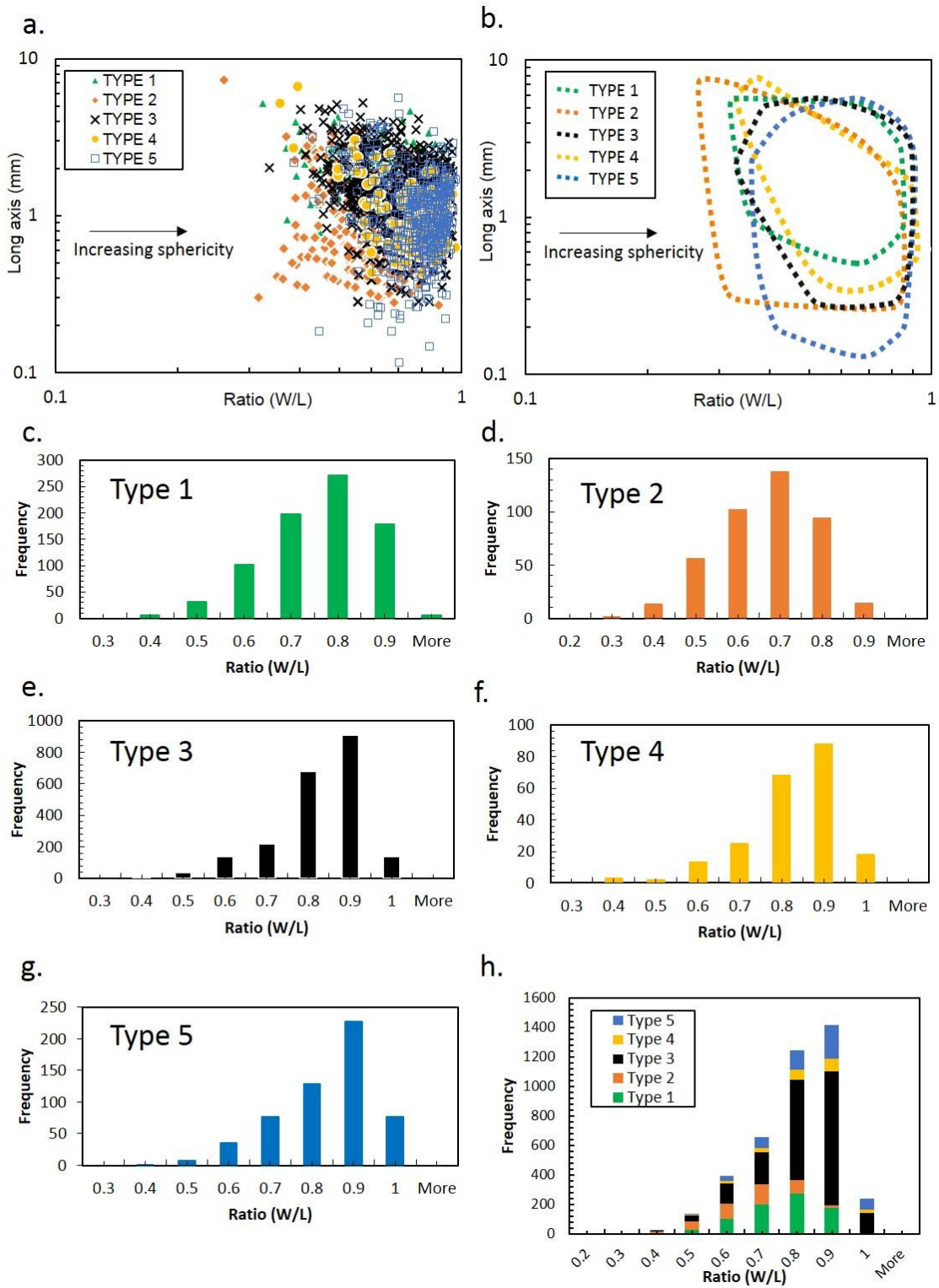
874

875

876

877

878



885 **TABLES**

886

887 Table 1: Spherulite crystal size distribution (CSD) parameters for sampled lava flows and domes. Calculated
 888 growth periods for spherulite growth are also shown in the table (small and large size fractions removed and
 889 calculated through the main body of the CSD). Growth period based on a growth rate of 6.33×10^{-7} (calculated by
 890 Castro et al., 2008).

Flow/ dome	No. of spherulites	Y intercept	Slope value	R ² value	Short axis	Int. axis	Long axis	Sphericity (%)	Growth period (days)
Pietre Cotte	999	4.7997	-8.5831	0.9826	1	1.4	2.8	56.3	2.1
Rocche Rosse	451	5.2683	-7.9464	0.9998	1	1.05	1.15	92.6	2.3
Grotta dei Palizzi	154	1.7185	-4.9954	0.9966	1	1.05	1.05	98.4	3.6
Forgia Vecchia	395	2.4416	-4.6717	0.9838	1	1.15	1.25	90.3	4
Pomiciazzo	255	-1.9983	-1.7524	0.9859	1	1.05	1.05	98.4	10.4
Capo Rosso	446	2.3387	-4.2148	0.9793	1	1	1.15	91.1	4.3
Castello	130	1.8541	-4.5033	0.9992	1	1	1	100	4.1
Punta di Costa	431	2.1136	-4.1954	0.9933	1	1.05	1.05	98.4	4.4
Monte Giardina	326	2.3264	-2.5891	0.9489	1	1	1	100	7.1
Falcone (rhyolite)	576	-1.4589	-2.0418	0.9943	1	1.05	1.1	95.4	8.9
Falcone (dacite)	1086	1.2866	-3.3478	0.9912	1	1.05	1.05	98.4	5.5
Punta del Perciato	156	1.0329	-3.2901	0.9717	1	1	1	100	5.6

891